

Bioinorganic Chemistry

How to cite: *Angew. Chem. Int. Ed.* **2020**, 59, 12965–12975

International Edition: doi.org/10.1002/anie.202003621

German Edition: doi.org/10.1002/ange.202003621

K β X-Ray Emission Spectroscopic Study of a Second-Row Transition Metal (Mo) and Its Application to Nitrogenase-Related Model Complexes

Rebeca G. Castillo, Justin T. Henthorn, Jeremy McGale, Dimitrios Maganas, and Serena DeBeer*

Abstract: In recent years, X-ray emission spectroscopy (XES) in the K β (3p-1s) and valence-to-core (valence-1s) regions has been increasingly used to study metal active sites in (bio)inorganic chemistry and catalysis, providing information about the metal spin state, oxidation state and the identity of coordinated ligands. However, to date this technique has been limited almost exclusively to first-row transition metals. In this work, we present an extension of K β XES (in both the 4p-1s and valence-to-1s [or VtC] regions) to the second transition row by performing a detailed experimental and theoretical analysis of the molybdenum emission lines. It is demonstrated in this work that K β_2 lines are dominated by spin state effects, while VtC XES of a 4d transition metal provides access to metal oxidation state and ligand identity. An extension of Mo K β XES to nitrogenase-relevant model complexes shows that the method is sufficiently sensitive to act as a spectator probe for redox events that are localized at the Fe atoms. Mo VtC XES thus has promise for future applications to nitrogenase, as well as a range of other Mo-containing biological cofactors. Further, the clear assignment of the origins of Mo VtC XES features opens up the possibility of applying this method to a wide range of second-row transition metals, thus providing chemists with a site-specific tool for the elucidation of 4d transition metal electronic structure.

Introduction

Molybdenum plays crucial roles in biological, geochemical, and catalytic cycles.^[1–7] Enzymatic systems containing molybdenum are responsible for a wide variety of catalytic functions, including oxygen atom transfer and hydroxylation

reactions, as well as the mediation of oxidation/reduction reactions in nitrogen, sulfur, and carbon metabolism. In most of the preceding cases, the catalytically active sites are comprised of mononuclear Mo atoms coordinated by a tricyclic pterin cofactor.^[7,8] To date, only two Mo enzymes have been identified that do not incorporate a pterin cofactor—the Mo-dependent nitrogenases, which utilize a Mo–7Fe–9S–C cluster to effect nitrogen reduction,^[9,10] and the orange protein, which contains a unique heterometallic Mo–Cu sulfide cluster of unknown function.^[11]

Mo K-edge X-ray absorption spectroscopy (XAS) and extended X-ray absorption fine structure (EXAFS) studies have had a significant impact on our understanding of the geometric and electronic structure of the active sites in Mo-containing enzymes.^[12–24] However, Mo K β X-ray emission spectroscopy (XES) of enzymatic systems has yet to be explored, and relatively little K β XES has been reported for any of the 4d transition metals (TMs).^[25–28] This is in stark contrast to 3d TMs, where K β XES has been utilized for the entire 1st transition series^[26,29–37] and applied in a wide range of fields, including homogenous and heterogeneous catalysis, materials science, geochemistry, and bioinorganic chemistry.^[32,36,38–48] K β XES of 1st row TMs has seen increasing use as an experimental probe of both metal spin state, based on the K β mainlines (3p-1s) region, and local coordination environment, based on the valence-to-core (VtC, ligand to 1s) region.

However, parallel studies on 4d TM complexes are exceedingly limited. Herein, we perform a detailed K β XES study on a series of Mo complexes, shown in Figure 1 and Table 1. While this work is mainly focused on Mo K β XES, we also present Mo K β_1 high-energy resolution fluorescence detected (HERFD) XAS as a complementary electronic structure probe.

In order to better understand the significance of the results presented here, it is useful to first briefly summarize the previous K β XES work done on 3d TMs and to compare this to the existing assignments for K β XES on 4d TMs.

X-ray emission spectroscopy, 1st vs. 2nd row transition metals. Figure 2 shows a comparison between the emission lines of 3d (A) and 4d (B) TMs. Figure 2A includes the well-established emission lines in increasing energy order: K α_2 , K α_1 , K β' , K $\beta_{1,3}$ and the VtC transitions (K β'' and K $\beta_{2,5}$). A representative energy level diagram is displayed below the emission spectrum in Figure 2C. Figure 2C shows the non-resonant emission processes that result from the ionization of the 1s core electron to the continuum. The analogous processes for 4d TMs are shown in Figure 2B and D. In the

[*] R. G. Castillo, J. T. Henthorn, J. McGale, S. DeBeer
Department of Inorganic Spectroscopy, Max Planck Institute for
Chemical Energy Conversion
Stiftstrasse 34–36, 45470 Mülheim an der Ruhr (Germany)
E-mail: serena.debeer@cec.mpg.de

D. Maganas
Max-Planck-Institut für Kohlenforschung
Kaiser-Wilhelm-Platz 1, 45470 Mülheim an der Ruhr (Germany)

Supporting information and the ORCID identification number(s) for the author(s) of this article can be found under <https://doi.org/10.1002/anie.202003621>.

© 2020 The Authors. Published by Wiley-VCH Verlag GmbH & Co. KGaA. This is an open access article under the terms of the Creative Commons Attribution License, which permits use, distribution and reproduction in any medium, provided the original work is properly cited.

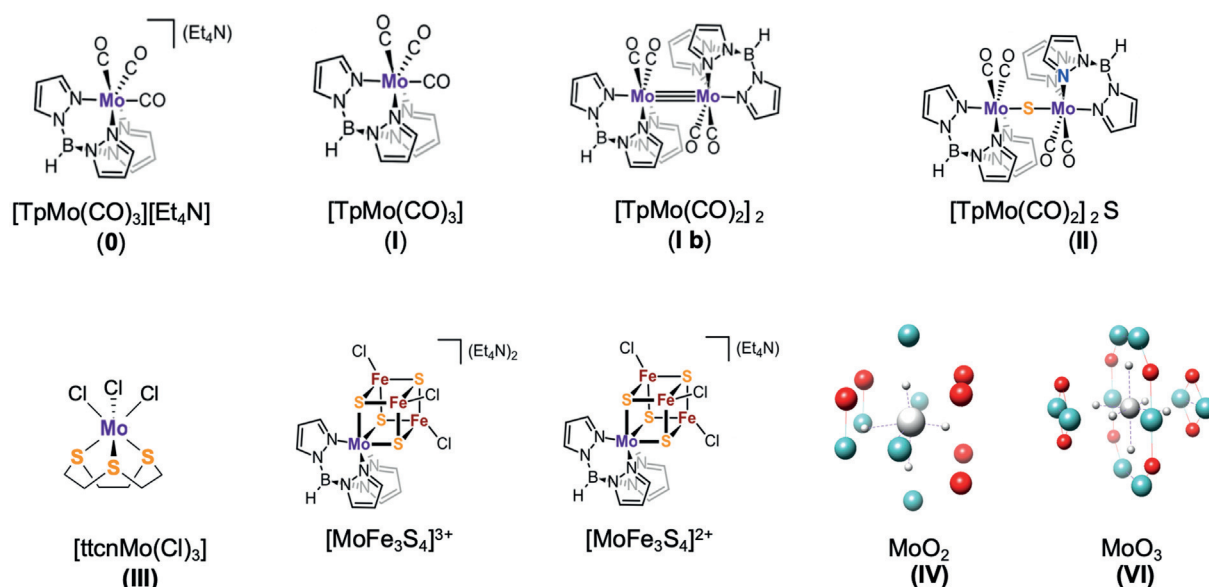


Figure 1. Model compounds investigated in the present study.

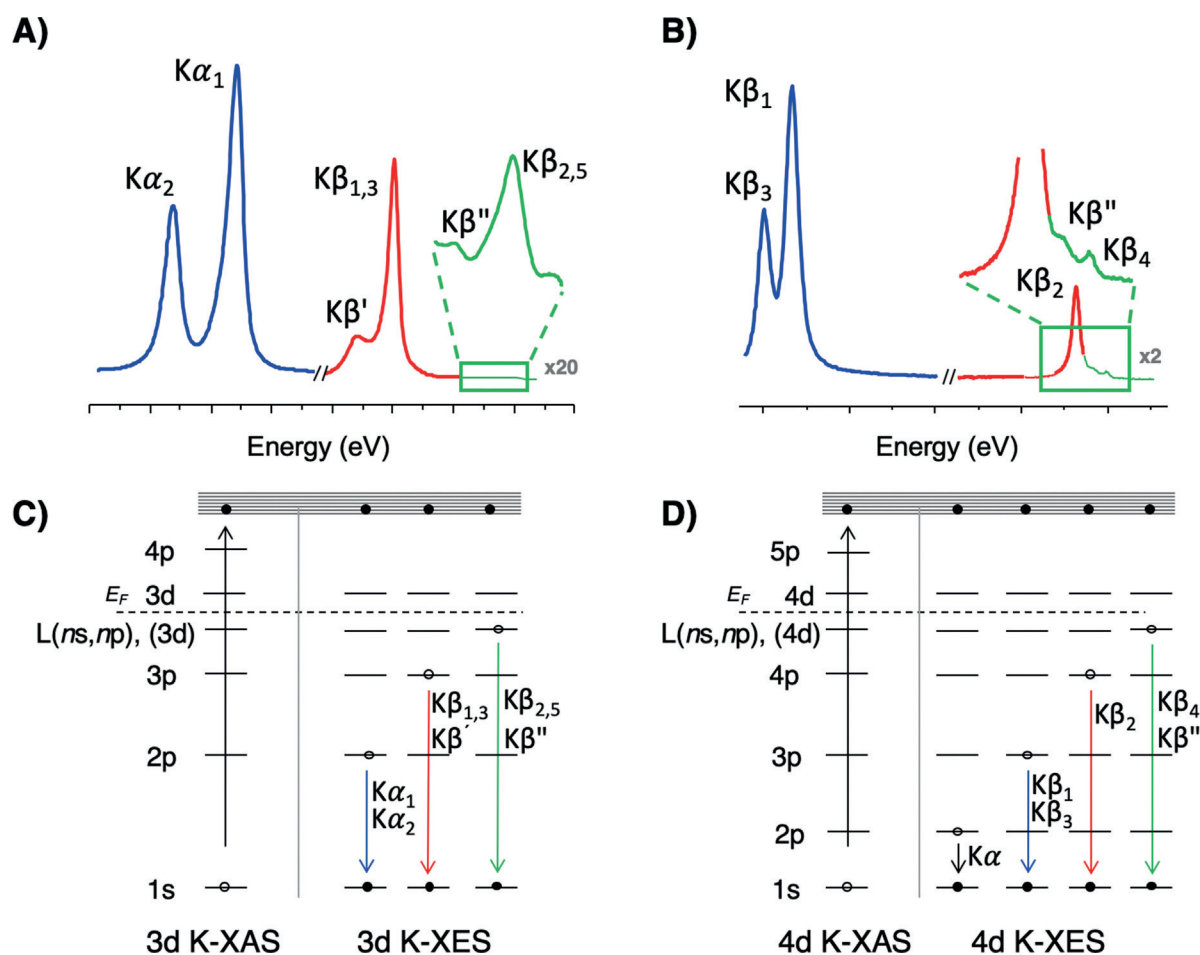


Figure 2. X-ray emission spectra and energy level diagrams of the absorption and emission processes for 3d (A and C) and 4d (B and D) TMs.

present study, we focus on the $K\beta_3$, $K\beta_1$, $K\beta_2$, $K\beta''$, and $K\beta_4$ emission lines, in increasing energy order.

The $K\beta_1$ and $K\beta_3$ emission lines in Mo XES correspond to the electric dipole allowed $3p \rightarrow 1s$ transitions. The splitting of these features is due to $3p$ core hole spin-orbit coupling

Table 1: Oxidation states and spin states of model complexes investigated in this study.

Compound (label)	Mo Oxidation state	Mo local spin state
[TpMo(CO) ₃][Et ₄ N] (0)	0	0
[TpMo(CO) ₃] (I)	I	1/2
[TpMo(CO) ₂] ₂ (Ib)	I, I	1/2, 1/2
[Tp ₂ Mo ₂ (CO) ₄](μ-S) (II)	II, II	1, 1
[ttcnMo(Cl) ₃] (III)	III	3/2
[MoFe ₃ S ₃] ³⁺	III	1/2
[MoFe ₃ S ₃] ²⁺	III	1/2
[MoO ₂] (IV)	IV	1
[MoO ₃] (VI)	VI	0

(SOC, ≈ 18 eV splitting). This may be contrasted with the $K\beta$ mainline XES of the 3d TMs, which splits into $K\beta_{1,3}$ and $K\beta'$ features predominantly due to 3p–3d exchange coupling, with the 3p SOC (< 1 eV) remaining as only a minor perturbation.

To ≈ 300 eV higher in energy there is the Mo $K\beta_2$ emission line, which arises from a 4p to 1s transition. The final state of the $K\beta_2$ decay process has a hole in the 4p shell, which interacts with the unpaired electrons in the 4d shell. Hence, the $K\beta_2$ line for 4d TMs is analogous to the $K\beta_{1,3}$ emission line for 3d TMs. However, 4d TM $K\beta_2$ XES spectra do not exhibit well-resolved splitting due in part to the smaller 4d–4p exchange integrals, relative to 3p–3d exchange integrals. In addition, the spectrum is further modulated relative to 3d TMs due to 1) the 4p⁵ final state SOC of a 4d TM being larger than the corresponding 3p⁵ final state SOC for 3d TMs and 2) the increased 1s core-hole lifetime broadening of 4d TMs relative to 3d TMs (1.2 eV for Fe and 4.52 eV for Mo).^[49]

VtC XES results from electrons in primarily ligand-based valence orbitals refilling the 1s core hole at the metal with the intensity due to the percent *np* metal character mixed into the valence orbitals.^[34,37] In 3d TMs, the $K\beta''$ results from ligand *ns* to metal 1s transitions, while the $K\beta_{2,5}$ results from ligand *np* to metal 1s transitions. In principle, analogous transitions should exist for the 4d TMs, and based on the energetics, these should be the $K\beta''$ and $K\beta_4$ transitions. Recently, Ravel et al. demonstrated that this analogy holds for the $K\beta''$ features in niobium complexes,^[25] where the energy of the $K\beta''$ features were shown to depend on ligand identity. In contrast, the $K\beta_4$ feature remains relatively unexplored, and previous studies have assigned it as arising from orbitals possessing primarily metal 4d character, rather than a ligand *np* to metal 1s transition.^[27] It is clear that a more detailed exploration as to the exact origin of the $K\beta_4$ features is warranted.

Herein, we carry out a systematic study of molecular Mo complexes and examine how the local geometric and electronic structures impact the Mo $K\beta_2$, $K\beta''$, and $K\beta_4$ features. The results are correlated to density functional theory (DFT) calculations in order to obtain more detailed insight. Complexes **0–VI** (Table 1, Figure 1) will first be presented to provide a detailed description of the Mo emission lines. We then utilize Mo $K\beta$ XES together with Mo $K\beta$ HERFD XAS to contrast the sensitivity of XES and XAS approaches for understanding electronic structural changes in two nitrogenase FeMoco related model complexes. The results allow for a better understanding of the origins of 4d TMs emission

lines and also establish the utility of Mo XES for future applications in bioinorganic chemistry and catalysis.

Results and Discussion

Mo $K\beta$ XES. The normalized Mo $K\beta$ XES spectra of compounds **0–VI** are presented in Figure 3 (top). The spectra consist of an intense $K\beta_2$ feature at ≈ 19970 eV and weaker higher energy peaks in the range of 19980–20003 eV representing the VtC region ($K\beta''$ and $K\beta_4$).

$K\beta_2$ XES. Figure 3 (bottom) shows an expansion of the $K\beta_2$ feature. The $K\beta_2$ spectra were fit with three pseudo-Voigt function line shapes, where Peak 1 (Table 2) is the dominant curve and well-represents the energy of the most intense feature. The vertical line at 19966.1 eV in Figure 3 (bottom) corresponds to the energy position of **0** at the $K\beta_{2\max}$ (Fit Peak 1 in Table 2). The energy position of the $K\beta_{2\max}$ (Peak 1) is found within a narrow range from 19966.1 and 19966.6 eV for all compounds with the exception of (ttcn)MoCl₃, compound

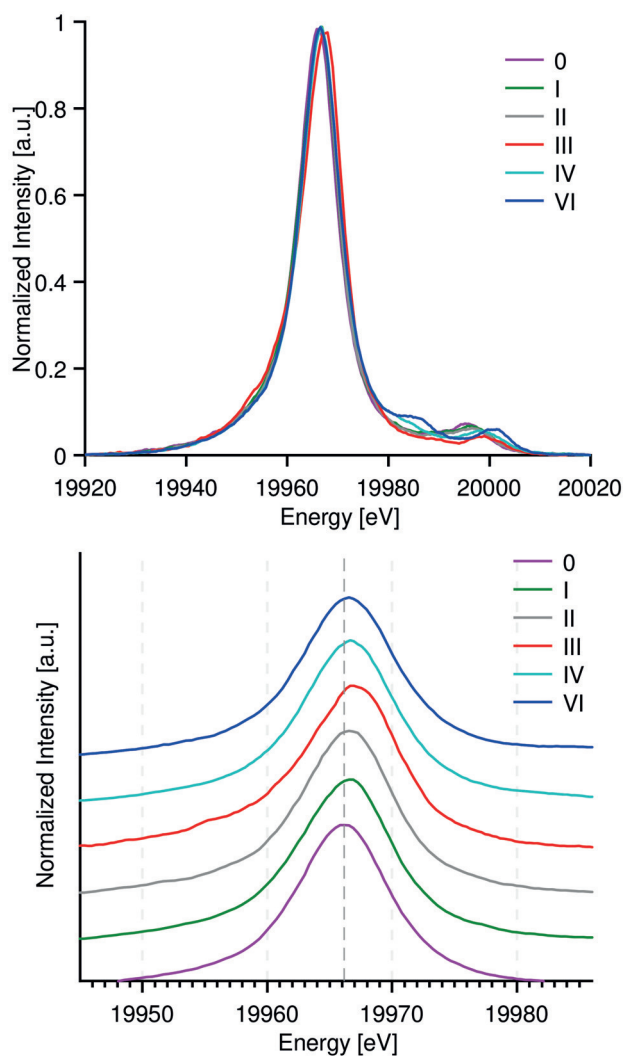


Figure 3. Mo $K\beta$ XES spectra of compounds **0–VI** (top) and zoom of the $K\beta_2$ region (bottom). Data presented with the intensity normalized to the $K\beta_2$ maxima.

Table 2: Interpretive pseudo-Voigt fits of Mo K β XES with the corresponding position (Pos.) and Amplitude (Amp.) of the peaks.

Complex	Total spin state	K $\beta_{2\max}$ Peak 1		K β'' Peak 2		Peak 3		K β_4 Peak 4		Peak 5	
		Pos. [eV]	Amp.	Pos. [eV]	Amp.	Pos. [eV]	Amp.	Pos. [eV]	Amp.	Pos. [eV]	Amp.
0	0	19966.1	12.75	19981.4	0.17	19989.7	0.12	19994.2	0.14	19997.4	0.28
I	1/2	19966.4	12.70	19980.2	0.15	19990.0	0.20	19995.2	0.15	19998.8	0.24
II	0	19966.5	12.46	19980.2	0.15	19990.7	0.19	19995.4	0.14	19999.0	0.19
III	3/2	19967.2	12.12	19983.7	0.06	19990.9	0.08	19997.5	0.11	20001.3	0.11
IV	1	19966.6	13.16	19981.5	0.22	19988.7	0.13	19997.2	0.22	20001.6	0.14
VI	0	19966.5	13.25	19983.1	0.34	19987.1	0.30	19999.0	0.22	20002.4	0.13

III, for which the K $\beta_{2\max}$ is at 19967.2 eV. As the K β_2 feature corresponds to a 4p to 1s transition with a 4p⁵4dⁿ final state, it will be influenced by 4p–4d exchange coupling, and thus should be sensitive to the number of unpaired 4d electrons. The $S = 3/2$ compound **III**, appears at highest energy due to the high-spin d³ configuration.

Using the isostructural models **0** and **I** for comparison, the energy of the K $\beta_{2\max}$ increases by ≈ 0.3 eV per unpaired electron for all $S \leq 1$ complexes. The apparent, albeit, small shifts in the K β_2 emission energy as a function of Mo oxidation-state clearly demonstrates the contribution of 4p–4d exchange coupling. However, this trend is significantly smaller than the 0.5–0.7 eV shift per unpaired electron shifts observed for 3d TMs.^[50–52] This is a result of the smaller 4p–4d exchange integrals relative to the corresponding 3p–3d integrals.^[53] We note that the shift will, of course, be further modulated by changes in the Mo 1s energy.

Although the shifts in the K β_2 maxima are modest, the fits reveal an asymmetric profile in the K β_2 feature (Table S1 and Figure S1), consistent with previous reports by Hoszowska et al.^[28] Due to the significant 1s core hole broadening for Mo, the position and intensity of the low energy shoulder is not well-defined. However, we can discuss the possible origins of this asymmetry based on Russel Sanders terms in the atomic limit, in a similar fashion as previously done for 3d TM.

For 3d TMs, it is well-established that the K $\beta_{1,3}$ spectral shape, including the K β' intensity, is dominated by the final state multiplet structure.^[50,52,54] More specifically, previous systematic studies of the contribution of the Slater–Condon parameters $F_{dd}^{2,4}$, F_{pd}^2 and $G_{pd}^{1,3}$ have shown that the p–d exchange integrals $G_{pd}^{1,3}$ dominate the spectral shape of 3d TMs. In order to assess whether or not a similar picture can be assumed for 4d TMs, we calculated the K $\beta_{1,3}$ and K β_2 XES spectra of Cr³⁺ and Mo³⁺, respectively (Figure S2), using ligand field multiplet calculations. The Slater–Condon parameters $F_{dd}^{2,4}$, F_{pd}^2 and $G_{pd}^{1,3}$ were individually varied between 100 and 50% of their atomic values. The F_{pd}^2 and $F_{dd}^{2,4}$ parameters were shown to result in only minor perturbations for the Cr³⁺ spectra, and made essentially no contributions to the Mo³⁺ spectra. In contrast, the p–d exchange integral ($G_{pd}^{1,3}$) has a pronounced effect on the spectral shape for both Cr³⁺ and Mo³⁺. This agrees with previous interpretations of 3d TM XES,^[49] and indicates that K β_2 spectra are dominated by 4p–4d exchange. We thus use this simple picture for further discussion of the spectral trends.

Examination of the fits reveals that compound **III** exhibits the greatest redistribution of intensity to lower energy, again consistent with increased 4p–4d exchange contributions for an $S = 3/2$ complex relative to the $S = 0$ to 1 complexes. This exchange interaction redistributes the multiplet intensity into two families of features, corresponding mainly to final state triplet and quintet states, as indicated in Table 3. The remaining compounds exhibit more comparable intensity distributions, consistent with the reduced d-counts and the presence of π -accepting carbonyl ligands in **0**, **I** and **II**, which results in delocalization of d-character onto ligand π^* orbitals.

Table 3: Russel Sanders Terms ($2S + 1L$) for the XES process in compounds 0 to IV. All complexes are in a low spin configuration.

Comp	4d ⁿ	GS ($1s^2 4d^n$)	IS ($1s^1 4d^n$)	FS ($1s^2 4p^5 4d^n$)
0	d ⁶	¹ I (¹ A _{1g})	² I	² H, ² I, ² K
I	d ⁵	² I (² T _{2g})	^{1,3} I	^{1,3} H, ^{1,3} I, ^{1,3} K
II	d ⁴	³ H (³ T _{1g})	^{2,4} H	^{2,4} G, ^{2,4} H, ^{2,4} I
III	d ³	⁴ F (⁴ A _{2g})	^{3,5} F	^{3,5} D, ^{3,5} F, ^{3,5} G
IV	d ²	³ F (³ T _{1g})	^{2,4} F	^{2,4} D, ^{2,4} F, ^{2,4} G

In order to understand the observed relatively modest changes in Mo K β_2 compared to the reported effect of d-count on the K $\beta_{1,3}$ lines of 3d TMs, NEVPT2 CASSCF calculations were performed on Mo³⁺ and Cr³⁺ free ions. The XES final state $1s^2 np^5 nd^n$ can be reached in the 1st excited state of a p→d CASSCF calculation utilizing a $1s^2 np^6 nd^{n-1}$ ground state. This first excited state will correspond to all multiplets allowed for $np^6 nd^{n-1} \rightarrow np^5 nd^n$, from where only the multiplets that correspond to the final states XES processes were selected. The calculated XES final states (without SOC contributions) are shown in Figure 4, with the ³T states shown in blue and the ⁵T states shown in red. The CASSCF + NEVPT2 calculations for Group 6 Cr³⁺ and Mo³⁺ ions have the same dipole-allowed XES final states. However, the final state XES multiplet energy distribution between these ions exhibits striking differences. In the case of Cr³⁺, the allowed XES final states span ≈ 23 eV, while for Mo³⁺ the final states span only ≈ 17 eV.

The decreased p–d exchange contribution to the K β_2 spectra of 4d TMs relative to that observed in the K $\beta_{1,3}$ spectra of 3d TMs is due to the increased delocalization of the 4d electrons. The inclusion of SOC in these calculations, and its influence on the $1s^2 np^5 nd^3$ final states, are included in Figure S3A,B. The energy span of the final states remains

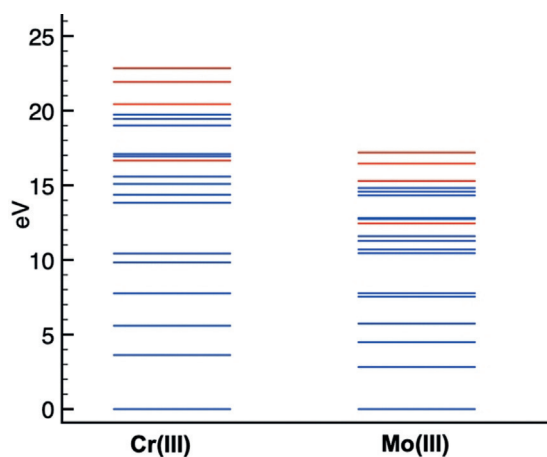


Figure 4. Calculated energy scheme for the allowed final states np^5nd^3 in the XES process (for Cr^{3+} vs. Mo^{3+} ; $^3,^5D$, $^3,^5F$, and $^3,^5G$ (color coded red for 5T states and blue for 3T states). Energy multiplet diagrams on different oxidation states included in the SI.

almost the same in Cr^{3+} with a small growth of 0.06 eV, while there is a 1.5 eV increase in the energy expansion of the final states for Mo^{3+} .

Hence, there is a total of 4.5 eV difference between the splitting of the final states for Cr^{3+} and Mo^{3+} , of which only 20% is due to spin-orbit coupling. The many calculated final state multiplets including SOC appear closer in energy and blur the ability to separate exchange-split multiplets, contributing to the asymmetric profile found in $\text{Mo K}\beta_2$.

A similar computational study was used to investigate the distribution of final states by varying the oxidation state. Figure S4 A,B shows an increase in the energy spread of the XES final states by ≈ 2.5 eV on going from Mo^{1+} ($S = 1/2$) to Mo^{2+} ($S = 1$) and by ≈ 5 eV on going from Mo^{2+} to Mo^{3+} ($S = 3/2$). This suggests an expansion of ≈ 2.5 eV per unpaired electron in the purely ionic limit. Due to delocalization of d-character onto the ligands, however, the effect is expected to diminish. This is clearly seen in the case of the carbonyl coordinated compounds where changes in spin state are effectively not observed at the $\text{K}\beta_2$ line due to the strong π -accepting nature of the ligand, as noted above and also previously observed in the $\text{K}\beta_{1,3}$ mainline of 3d TMs.^[55]

Mo valence-to-core $\text{K}\beta_4$ and $\text{K}\beta''$. Resolved but far less intense $\text{K}\beta_4$ and $\text{K}\beta''$ transitions appear on the high-energy tail of the $\text{K}\beta_2$ mainline. Together, these transitions make up the Mo VtC region as shown in Figure 5 (top). If we assume that the classical 3d TMs VtC transition assignments are transferable to the Mo VtC, the following hypothetical assignments can be made:

- 1) The $\text{K}\beta_4$ feature is primarily due to transitions from np ligand valence orbitals to the metal $1s$ core hole. The intensity of this feature is dominated by the amount of metal p character mixed into these valence orbitals. The $\text{K}\beta_4$ feature is the equivalent of the $L(np) \rightarrow M(1s)$ $\text{K}\beta_{2,5}$ feature for 3d TMs, where the intensities of the peak have been previously correlated with the $M-L$ bond length
- 2) The Mo $\text{K}\beta''$ peak is primarily due to transitions from ns ligand valence orbitals to the metal $1s$ core hole. It is

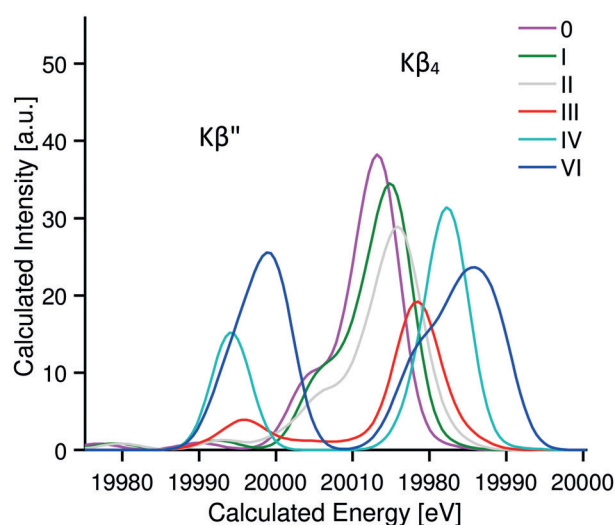
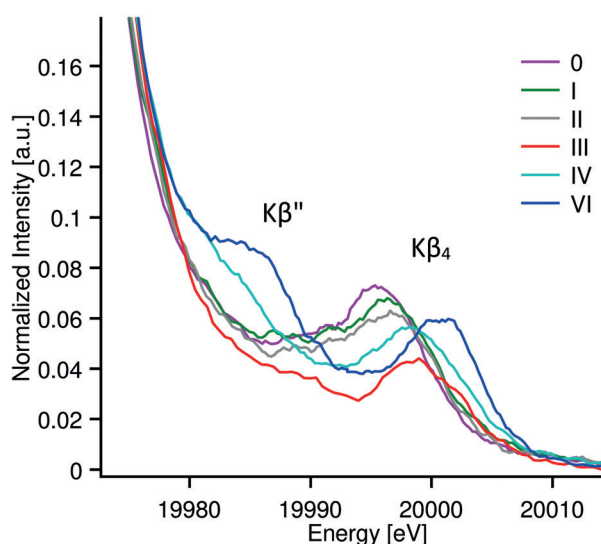


Figure 5. Experimental (Top) and calculated (bottom) VtC XES spectra for compounds **0–VI**.

dominated by ligand identity and the intensity is modulated by metal–ligand bond length.^[27]

Experimental data were fit for all compounds, including the main peak positions and amplitudes, and are included in Table 2. The most intense peaks correspond to the $\text{K}\beta_4$ features, located between 1995–2010 eV for compounds **0** to **VI**, with total areas of 0.2–0.4 as indicated in Table 2 (Peak 4 and Peak 5). The energy of the $\text{K}\beta_4$ feature appears to track with oxidation state, with the feature increasing in energy by ≈ 5 eV on going from **0** to **VI**. This likely reflects, in large part, the stabilization of the Mo $1s$ energy upon increasing Z_{eff} . Similar trends have been previously observed for 3d TM.^[56]

As the weak $\text{K}\beta''$ features appear on the high-energy tail of the more intense $\text{K}\beta_2$ mainline, the $\text{K}\beta''$ features are either obscured or poorly resolved (between 1975–1990 eV, Peaks 2 and 3, Table 2). However, for the molybdenum oxides **IV** and **VI** relatively intense $\text{K}\beta''$ features are observed.

To further test the assignment of these transitions and gain additional insight into their molecular origin, the Mo VtC of

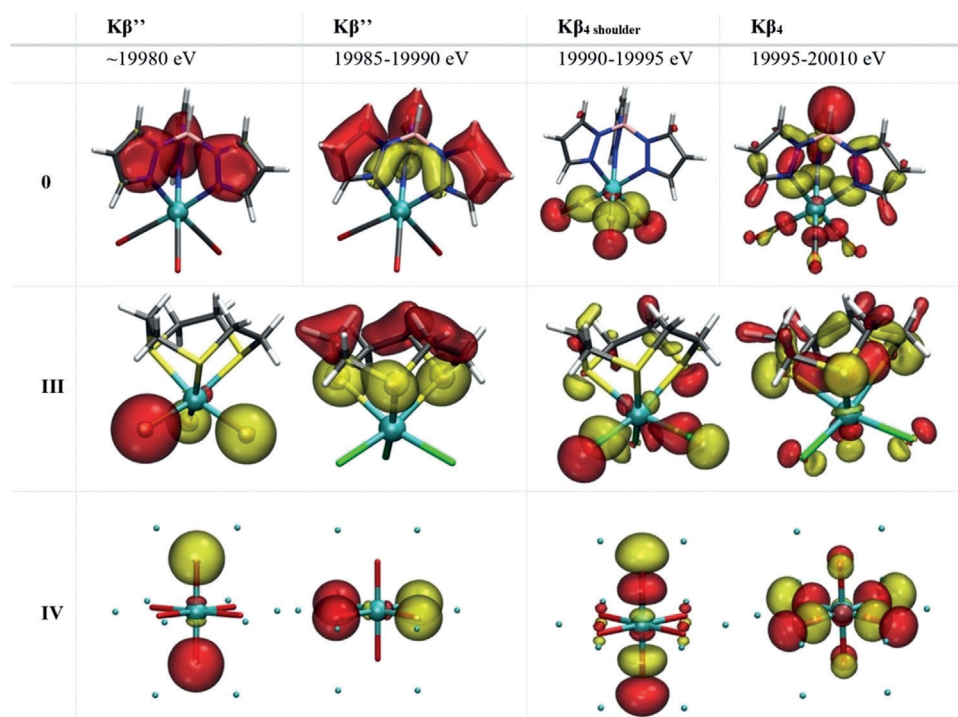


Figure 6. MOs involved in the most intense $K\beta''$ and $K\beta_4$ transitions for compounds **0**, **III**, and **IV**.

each compound was calculated by ground-state DFT methods.^[34] The calculated VtC spectra were obtained by allowing for electric dipole, magnetic dipole and quadrupole contributions. The resultant spectra were found to be comprised of 99.9% dipole contributions. The DFT results well-reproduce the experimental data, replicating the observed energy trends and transition intensities (Figure 5, bottom). The calculated spectra allow the donor molecular orbitals of each transition to be assigned. Figure 6 shows the primary contributing molecular orbitals (MO) for the $K\beta''$ and the more intense $K\beta_4$ transitions for compounds **0**, **III** and **IV**. A quantitative orbital analysis for all compounds is included in Table S2.

Qualitative inspection of the MOs contributing to the intensity of the $K\beta_4$ peak demonstrate that this transition is mainly from np ligand valence orbitals and that the calculated intensity is dominated by the amount of metal p character mixed into these valence orbitals. For instance, the most intense transition for **III** is in the $K\beta_4$ region and is attributed to a $Cl\ 3p \rightarrow Mo\ 1s$ transition ($\approx 19999.4\ eV$ with a total integrated area of 0.22 units Figure 6). The $K\beta_4$ transitions for both **IV** and **VI** are from $O\ 2p$ ligand MOs (Figure 5) with $Mo\ 4p/5p$ dipole contributions. As **IV** and **VI** each have oxygen ligands, but different d electron counts, their comparison most directly tests the $K\beta_4$ origin. The $K\beta_4$ energy positions for **IV** and **VI** are $\approx 1.3\ eV$ shifted and their total integrated areas are 0.36 and 0.33 units. It was previously suggested that the $K\beta_4$ feature is formally a $4d \rightarrow 1s$ transition.^[27] However, complex **VI** is formally d^0 with no available donor d -electrons for the $K\beta_4$ transition. Therefore, this further supports the assignment of the $K\beta_4$ feature as a ligand $np \rightarrow Mo\ 1s$ transition, which gains intensity through metal np character mixing into the ligand orbitals. Only complexes **III**, **IV**, and **VI**

have well-resolved $K\beta''$ features. The MOs which correspond to these transitions are ligand ns based. The calculated spectrum for complex **III** shows one main feature due to the $Cl\ 3s \rightarrow Mo\ 1s$ transition between 19987–19990 eV and contributions from the $ttcn$ ligand, found at 19990 eV but with low intensity. Calculated XES spectra of **IV** and **VI** show one main $K\beta''$ feature due mainly to $O\ 2s$ -based molecular orbitals. These transitions possess slightly different intensities due to varying $Mo-O$ distances. Complex **VI**, MoO_3 , has an orthorhombic crystal distorted bulk unit with strong anisotropy in $Mo-O$ bonding that is also responsible for a higher dipole contribution relative to the monoclinic MoO_2 complex **IV**. The shortest $Mo-O$ bond distance in MoO_3 is $1.67\ \text{\AA}$ while the shortest $Mo-O$ bond length for MoO_2 is $2.023\ \text{\AA}$. These calculations validate the aforementioned hypothesized transition assignments (see above).

The back-bonding character of the carbonyl ligands yields VtC transitions that are more mixed in character. The rich Fe VtC spectra of Fe carbonyl complexes exhibit features arising from $\sigma^* 2s-2s$ (CO) and $\sigma 2p_z-2p_z$ (CO) interactions with the metal.^[55] For the Mo carbonyl-containing compounds, well-resolved contributions from the carbonyl ligands are not observed. However, the calculations reproduce experimental trends, with the energy of the $K\beta_4$ increasing and the intensity decreasing going from **0** to **II**. The σ -type bonding interactions are capable of mixing with $Mo\ p$ orbitals to form available donor orbitals that are major contributors to the $K\beta_4$ region, Figure 6. The transitions in the $K\beta_4$ region with the highest dipole contribution to the emission oscillator strength correspond to transitions from $\sigma 2p_z-2p_z(CO) + \sigma N(Tp)$ MOs. The lessening of π back-donation from the $Mo\ 4d$ shell is reflected in $Mo-CO$ bond lengthening from **0** to **II**. The increase in $Mo-$

CO bond length affects the intensity of VtC features as the np Mo-ligand mixing decreases. This same distance dependence is observed in the $K\beta_{2,5}$ feature of 3d TMs.^[34,37]

For compounds **0** to **II**, three distinguishable peaks are found to be part of the $K\beta''$ calculated transitions. The two transitions between 19980–19985 eV are of significantly lower intensity than the other calculated $K\beta''$ features and not observed in the experimental data. The low intensity features are due to N and C 2s orbital delocalization over the tris(pyrazolyl)borate (Tp) ligand. From an MO description, both features can be assigned as transitions from MOs of the chelating pyrazole rings in the Tp ligand with little contribution of the $Mo(CO)_3$ fragment. The minimal amount of metal p character mixed into these MOs results in very small dipole contributions to the calculated oscillator strength. This explains why these transitions are not observed in the experimental spectra.

Despite the disparate ligand character of the studied Mo complexes, clear trends in the Mo VtC emerge: the $K\beta_4$ feature provides a marker of Mo oxidation-state and is sensitive to ligand identity and metal ligand bond length.

XAS measurements. Figure 7 displays the Mo $K\beta_1$ HERFD XAS of the complexes grouped by ligand identity,

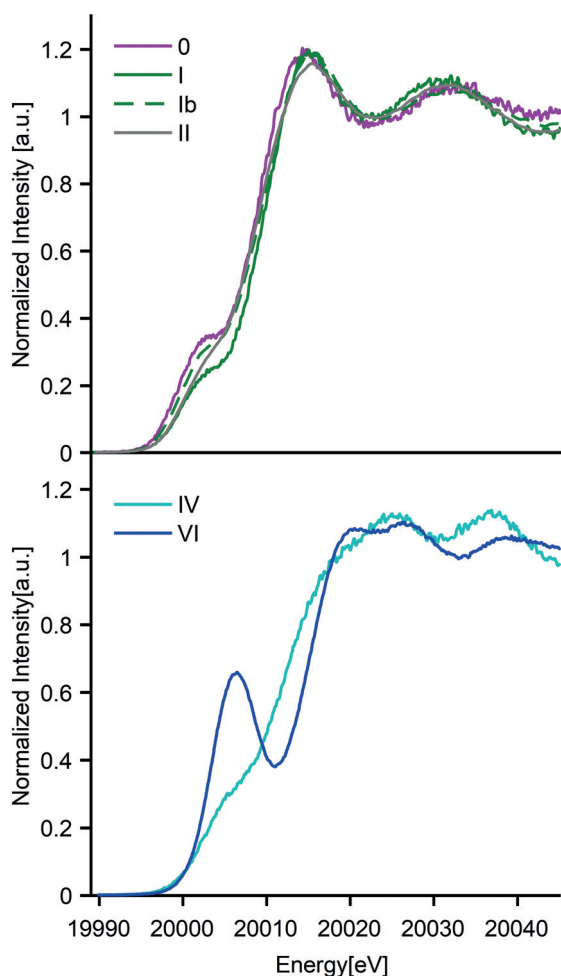


Figure 7. $K\beta_1$ HERFD XAS spectra of Mo compounds containing CO ligands **0** to **II** (top) and Mo oxides **IV** and **VI** (bottom).

with the Mo compounds with Tp and CO ligands (**0**, **I**, **Ib** and **II**) at the top and the oxides (**IV** and **VI**) at the bottom. Metal K-edge positions shift towards higher energies with increasing oxidation state, as the effective nuclear charge varies.^[57,58] Figure 7 (bottom) shows an energy shift of +2.6 eV in the rising edge on going from compound **IV** to **VI**. Figure 7 (top) shows a ≈ 1 eV energy shift at the white lines, consistent with the increase in oxidation state from **0** \rightarrow **I** \rightarrow **II**. However, identification of the Mo oxidation state of these compounds by the inflection points of their corresponding rising edges has a less intuitive interpretation. In this particular case, the rising edge of each compound is modulated by the strong back-bonding nature of the carbonyl ligands, with an increase in back-bonding resulting in an edge shift toward higher energy. Interestingly, for the present series, the $K\beta_4$ XES features seem to more clearly correlate with the oxidation states of the compounds than the rising edge positions.^[56]

A practical case: molybdenum–iron–sulfur clusters. Having established in the preceding sections the complementary information that can be obtained by the use Mo $K\beta$ XES and $K\beta_1$ HERFD XAS, we now go on to utilize these methods to understand synthetic MoFe cubanes.^[59] These serve as examples of more complex models with relevance to a biological system, in this particular case the FeMoco active site of nitrogenase. Two MoFe cubanes,^[59] $[MoFe_3S_4]^{3+}$ and $[MoFe_3S_4]^{2+}$, were studied to determine the sensitivity of each method to one electron cluster reductions. In addition, Fe $K\beta_{1,3}$ HERFD experiments are also presented in order to obtain insight into the location of the redox event.

Figure 8 displays both Mo and Fe $K\beta$ HERFD-XAS spectra. The Fe $K\beta_{1,3}$ HERFD-XAS in Figure 8 (bottom) shows a 0.7 eV decrease in the rising edge position on going from $[MoFe_3S_4]^{3+}$ to $[MoFe_3S_4]^{2+}$, indicating an iron-based reduction. Figure 8 (top) shows (tten)MoCl₃ compound **III** and both MoFe cubanes. While all three complexes contain a Mo^{3+} atom, complex **III** clearly is very different in edge shape and whiteline position. This may be attributed to the different ligation environment and the differences in local Mo spin state ($S = 3/2$ for **III** vs. $S_{loc}(Mo) = 1/2$ for the cubanes).^[60,61] Both MoFe cubanes overlap in the whiteline region of the Mo K-edge XAS spectra, suggesting there is no change in oxidation state at the Mo site. This is consistent with reduction occurring at the iron, as supported by the Fe K-edge data and previous Mössbauer studies.^[62] Just before the rising edge, both compounds **III** and $[MoFe_3S_4]^{2+}$ overlap in the pre-edge area, while $[MoFe_3S_4]^{3+}$ has a higher intensity pre-edge. This may reflect greater p–d mixing in the $[MoFe_3S_4]^{3+}$ cubane due to increased covalency and/or the presence of MMCT transitions.

Figure 9 displays the Mo $K\beta_2$ and VtC for **III** and both MoFe cubanes. The $K\beta_{2max}$ of compound **III** ($S = 3/2$) is found at 19967.2 eV while both MoFe cubanes ($S_{loc}(Mo) = 1/2$) show their $K\beta_{2max} \approx 0.6$ eV downshifted from the $K\beta_{2max}$ of **III**. This translates to a 0.3 eV energy shift per unpaired electron in Mo $K\beta_{2max}$, and is fully consistent with the shifts determined for compounds **0**–**VI**. We note, however, that the shift may also be attributed to an increase in covalency upon replacing the thioethers in **III** with the more covalent sulfides in the cubane clusters.^[50]

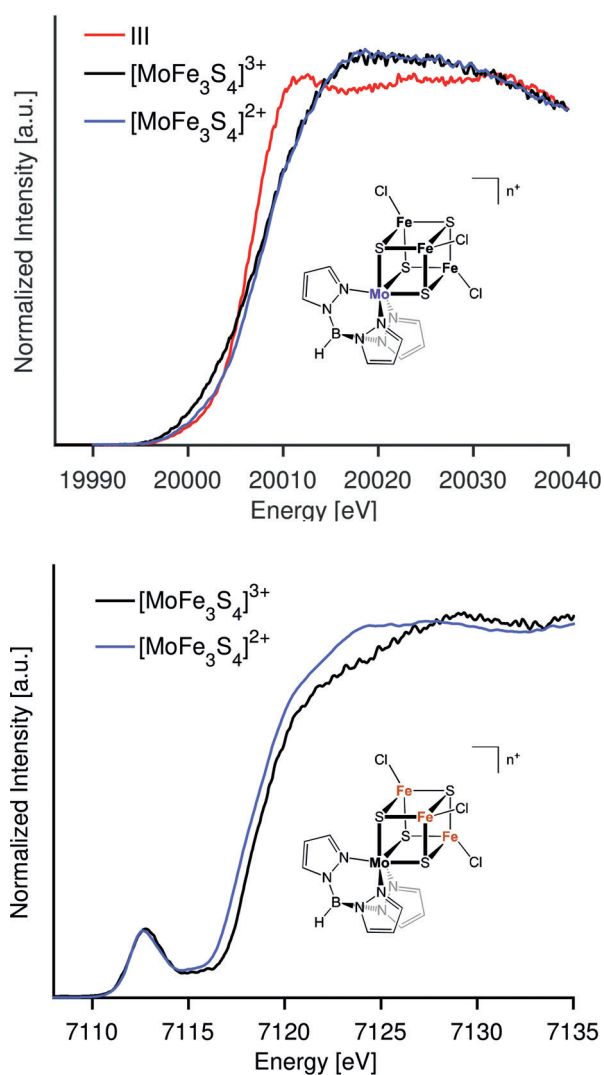


Figure 8. Mo $K\beta_1$ (top) and Fe $K\beta_{1,3}$ (bottom) HERFD XAS spectra of **III** (Mo only), $[\text{MoFe}_3\text{S}_4]^{3+}$ and $[\text{MoFe}_3\text{S}_4]^{2+}$.

Figure 9 (lower right) shows the enlarged $K\beta_{4\text{max}}$ region for all three complexes. $[\text{MoFe}_3\text{S}_4]^{2+}$ has a $K\beta_4$ maximum at 19998 eV, about 1 eV lower in energy than the $[\text{MoFe}_3\text{S}_4]^{3+}$ and (tcn)MoCl₃ $K\beta_{4\text{max}}$. Although MoFe cubanes share the same oxidation and spin state at the Mo site, differences in the $K\beta_4$ features suggest additional electronic structural contributions to this spectral region.

XES spectra were calculated by DFT in order to understand the origin of these differences (Figure 10, Figure 11). In both experimental and calculated spectra, compound **III** shows a $K\beta_4$ peak with lower intensity than the MoFe cubanes. In **III**, the intensity of this peak is mainly due to transitions from 3p Cl and thioether sulfur MOs (Figure 6). However, for both MoFe cubanes the origin of the $K\beta_4$ transitions is less straight forward as the calculated transitions are modulated by covalency (via Mo–S(thiolate) and Mo–Fe bonding). For the MoFe cubanes, the Mo–N(Tp) and Mo–S average distances decrease by 0.03 eV and 0.02 eV, respectively, going from $[\text{MoFe}_3\text{S}_4]^{2+}$ to $[\text{MoFe}_3\text{S}_4]^{3+}$. Furthermore, the MOs

involved in the $K\beta_4$ transitions show a decrease of 0.9% in Mo np character and an increase of 4% in Fe 3d character.

The putative effect of metal–ligand bonding on the XES VtC spectra of both cubanes was investigated by replacing the Fe sites with closed shell atoms without changing overall geometry or local Mo spin. Figure 11 shows the DFT calculated XES spectra for $[\text{MoFe}_3\text{S}_4]^{3+}$, $[\text{MoFe}_3\text{S}_4]^{2+}$ and their corresponding MoGaZn substituted cubanes: $[\text{MoGa}_2\text{ZnS}_4]^{3+}$ and $[\text{MoGaZn}_2\text{S}_4]^{2+}$ (with a Mo local spin of $1/2$). MoGaZn cubanes are hypothetical models that use MoFe cubane structure without computing optimization geometries. Comparisons with the real MoFe cubanes were made by shifting in energy the calculated MoGaZn spectra to align both $[\text{MoGa}_2\text{ZnS}_4]^{3+}$ and $[\text{MoFe}_3\text{S}_4]^{3+}$. Unlike the XES computed for the MoFe cubanes, the calculated energy position at the $K\beta_4$ maximum remains the same for both MoGaZn cubanes. These results demonstrate that the experimental Mo VtC XES of the MoFe cubanes is sensitive to the reduction occurring at the Fe site.

Since the ground states for $[\text{MoGa}_2\text{ZnS}_4]^{3+}$ and $[\text{MoGaZn}_2\text{S}_4]^{2+}$ have Mo local spins of $3/2$, XES spectra were also calculated for the $S_{\text{loc}}(\text{Mo}) = 1/2$ spin states. No energy shift was observed in the $K\beta_4$ peak position and the $K\beta_4$ intensity remained higher for the $[\text{MoGa}_2\text{ZnS}_4]^{3+}$ cubane (Figure S6).

This computational study demonstrates that Mo VtC is moderately sensitive to metal–metal interactions, but relatively insensitive to the Mo local spin state.

Conclusion

A systematic experimental and theoretical study of Mo $K\beta$ XES has been performed for a range of molecular and extended lattice Mo materials. The ability of this method to provide local information on Mo oxidation state, spin state, and identity of coordinated ligands has been established. The trends elucidated here should be readily transferable to other 4d TMs.

Having established the strong correlations between experimental and calculated Mo $K\beta$ XES spectra, the method was extended to MoFe₃ cubane clusters with relevance to the FeMo cofactor of nitrogenase. These studies highlight the ability of Mo $K\beta$ XES to report on subtle changes in cubane electronic structure. By combining the XES studies with XAS measurements at the Mo and Fe K-edge, it is demonstrated that the Mo $K\beta$ XES is sufficiently sensitive to show changes upon iron-based reduction. This suggests that Mo $K\beta$ XES could be useful for studies of FeMoco and might provide greater selectivity than Fe $K\beta$ XES, where contributions from the 7 iron of FeMoco and the 8 irons of the P-cluster greatly complicate the spectral interpretation.

The present study forms the basis for applying Mo $K\beta$ XES in homogeneous and heterogeneous catalysis. While Mo $K\beta$ XES suffers from relatively large Mo 1s core-hole lifetime broadening,^[22,27] this technique may be particularly useful for Mo-containing enzymes with a large number of S atoms present. Due to the overlap of the Mo L-edges and S K-edges, it is difficult to deconvolute the Mo and S contributions in the tender X-ray spectra.^[63]

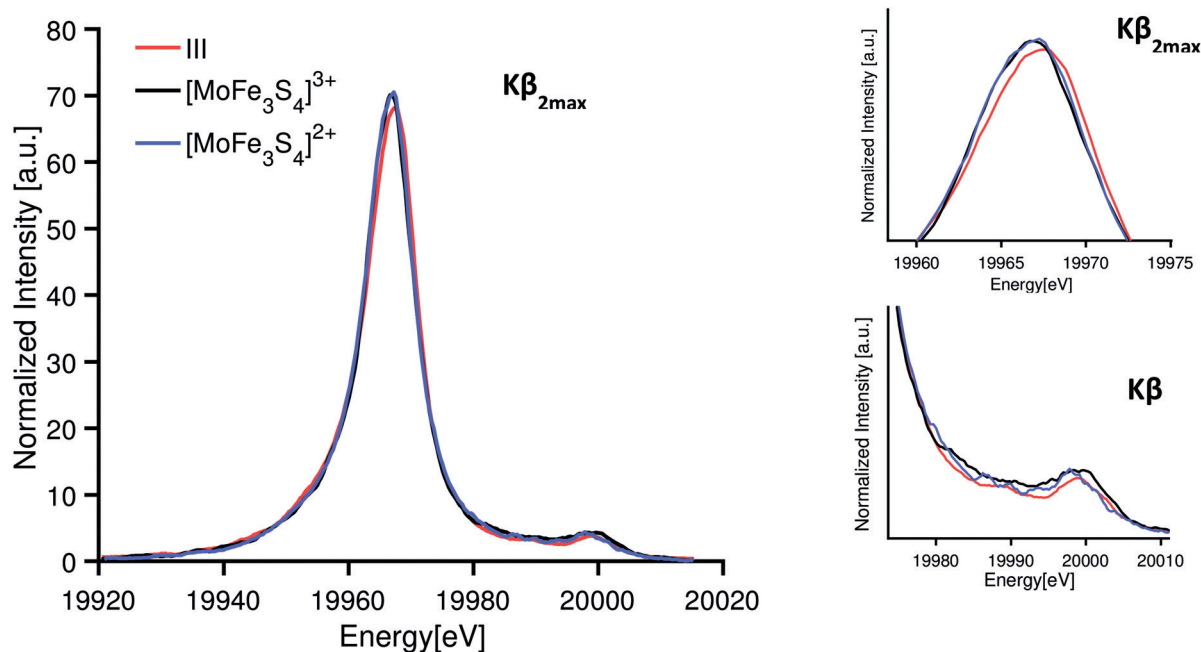


Figure 9. Mo $K\beta_2$ and $K\beta_4$ XES spectra of compounds III, $[\text{MoFe}_3\text{S}_4]^{3+}$, and $[\text{MoFe}_3\text{S}_4]^{2+}$. Plots at the right side contain both regions enlarged.

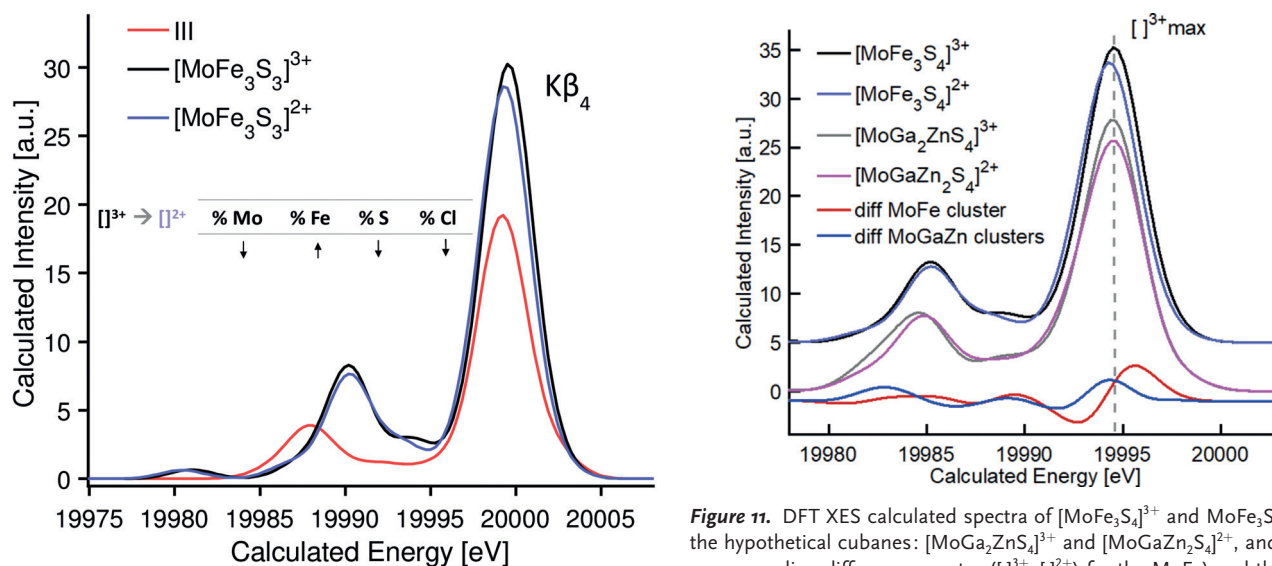


Figure 10. DFT XES calculated spectra of compounds III, $[\text{MoFe}_3\text{S}_4]^{3+}$, and $[\text{MoFe}_3\text{S}_4]^{2+}$.

The approach presented here may provide a means to more readily access electronic structural changes at the Mo in biological systems where molybdenum is involved either as a mononuclear active site (DMSO reductase, sulfite oxidase, etc) or as part of multinuclear metal centres, like Cu,Mo-containing CO dehydrogenases.^[64]

Acknowledgements

Financial support was provided by the Max Planck Society and the International Max Planck Research School (IMPRS)

Recharge. The authors also acknowledge the DFG project DE 1877/1-1 (S.D.) within the SPP 1927 “Iron-Sulfur for Life”. All presented X-ray data was collected at beamline ID-26 at the European Synchrotron Radiation Facility (ESRF), Grenoble, France. We are grateful to beamline scientists Dr. Sara LaFuerza and Dr. Blanka Detlefs for providing assistance in using beamline ID-26, and Dr. George Cutsail III and Dr. Benjamin Van Kuiken for support during beamtime. The authors also acknowledge Dr. George Cutsail III for critical reading of the manuscript. We thank Dr. Benjamin Cahier for insightful discussions and help regarding CASSCF NEVPT2 calculations, Zachary Mathe for guidance with embedding

procedures for the MoO₂ and MoO₃, and Albert Th. Thorhallsson and Ragnar Bjornsson for helpful discussions regarding the Mo–Fe–S clusters cubanes.

Conflict of interest

The authors declare no conflict of interest.

Keywords: molybdenum · nitrogenase · valence-to-core · X-ray emission spectroscopy

- [1] J.-H. Park, C.-H. Shin, *J. Ind. Eng. Chem.* **2015**, *21*, 683–688.
- [2] A. de Nazaré de Oliveira, M. A. Barbosa de Lima, L. H. de Oliveira Pires, M. Rosas da Silva, P. T. Souza da Luz, R. S. Angélica, G. N. da Rocha Filho, C. E. F. da Costa, R. Luque, L. A. Santos do Nascimento, *Materials (Basel)* **2019**, *12*, 1431.
- [3] W. Ripperger, W. Saum, *J. Less-Common Met.* **1977**, *54*, 353–362.
- [4] B. Grzybowska, J. Haber, J. Komorek, *J. Catal.* **1972**, *25*, 25–32.
- [5] A. Magalon, J. G. Fedor, A. Walburger, J. H. Weiner, *Coord. Chem. Rev.* **2011**, *255*, 1159–1178.
- [6] R. R. Mendel, *J. Biol. Chem.* **2013**, *288*, 13165–13172.
- [7] R. Hille, J. Hall, P. Basu, *Chem. Rev.* **2014**, *114*, 3963–4038.
- [8] L. J. Giles, C. Ruppelt, J. Yang, R. R. Mendel, F. Bittner, M. L. Kirk, *Inorg. Chem.* **2014**, *53*, 9460–9462.
- [9] B. M. Hoffman, D. Lukoyanov, Z.-Y. Yang, D. R. Dean, L. C. Seefeldt, *Chem. Rev.* **2014**, *114*, 4041–4062.
- [10] B. K. Burgess, D. J. Lowe, *Chem. Rev.* **1996**, *96*, 2983–3012.
- [11] M. S. P. Carepo, S. R. Pauleta, A. G. Wedd, J. J. G. Moura, I. Moura, *J. Biol. Inorg. Chem.* **2014**, *19*, 605–614.
- [12] H. H. Harris, G. N. George, K. V. Rajagopalan, *Inorg. Chem.* **2006**, *45*, 493–495.
- [13] P. D. Smith, D. A. Slizys, G. N. George, C. G. Young, *J. Am. Chem. Soc.* **2000**, *122*, 2946–2947.
- [14] S. P. Cramer, R. Hille, *J. Am. Chem. Soc.* **1985**, *107*, 8164–8169.
- [15] G. N. George, C. Costa, J. J. G. Moura, I. Moura, *J. Am. Chem. Soc.* **1999**, *121*, 2625–2626.
- [16] G. N. George, C. A. Kipke, R. C. Prince, R. A. Sunde, J. H. Enemark, S. P. Cramer, *Biochemistry* **1989**, *28*, 5075–5080.
- [17] S. P. Cramer, K. O. Hodgson, W. O. Gillum, L. E. Mortenson, *J. Am. Chem. Soc.* **1978**, *100*, 3398–3407.
- [18] J. Christiansen, R. C. Tittsworth, B. J. Hales, S. P. Cramer, *J. Am. Chem. Soc.* **1995**, *117*, 10017–10024.
- [19] G. N. George, J. Hilton, K. V. Rajagopalan, *J. Am. Chem. Soc.* **1996**, *118*, 1113–1117.
- [20] G. N. George, I. J. Pickering, C. Kisker, *Inorg. Chem.* **1999**, *38*, 2539–2540.
- [21] G. N. George, J. Hilton, C. Temple, R. C. Prince, K. V. Rajagopalan, *J. Am. Chem. Soc.* **1999**, *121*, 1256–1266.
- [22] R. Bjornsson, F. A. Lima, T. Spatzal, T. Weyhermüller, P. Glatzel, E. Bill, O. Einsle, F. Neese, S. DeBeer, *Chem. Sci.* **2014**, *5*, 3096–3103.
- [23] C. Van Stappen, R. Davydov, Z.-Y. Yang, R. Fan, Y. Guo, E. Bill, L. C. Seefeldt, B. M. Hoffman, S. DeBeer, *Inorg. Chem.* **2019**, *58*, 12365–12376.
- [24] L. J. Ingersol, J. Yang, K. Kc, A. Pokhrel, A. V. Astashkin, J. H. Weiner, C. A. Johnston, M. L. Kirk, *J. Am. Chem. Soc.* **2020**, *142*, 2721–2725.
- [25] B. Ravel, A. J. Kropf, D. Yang, M. Wang, M. Topsakal, D. Lu, M. C. Stennett, N. C. Hyatt, *Phys. Rev. B* **2018**, *97*, 125139.
- [26] C. J. Clarke, S. Hayama, A. Hawes, J. P. Hallett, T. W. Chamberlain, K. R. J. Lovelock, N. A. Besley, *J. Phys. Chem. A* **2019**, *123*, 9552–9559.
- [27] C. J. Doonan, L. Zhang, C. G. Young, S. J. George, A. Deb, U. Bergmann, G. N. George, S. P. Cramer, *Inorg. Chem.* **2005**, *44*, 2579–2581.
- [28] J. Hozzowska, J. C. Dousse, *J. Phys. B* **1996**, *29*, 1641–1653.
- [29] E. Gallo, C. Lamberti, P. Glatzel, *Phys. Chem. Chem. Phys.* **2011**, *13*, 19409–19419.
- [30] O. V. Safonova, L. N. Vykhodtseva, N. A. Polyakov, J. C. Swarbrick, M. Sikora, P. Glatzel, V. A. Safonov, *Electrochim. Acta* **2010**, *56*, 145–153.
- [31] S. G. Eeckhout, O. V. Safonova, G. Smolentsev, M. Biasioli, V. A. Safonov, L. N. Vykhodtseva, M. Sikora, P. Glatzel, *J. Anal. At. Spectrom.* **2009**, *24*, 215–223.
- [32] J. A. Rees, A. Wandzilak, D. Maganas, N. I. C. Wurster, S. Hugenbruch, J. K. Kowalska, C. J. Pollock, F. A. Lima, K. D. Finkelstein, S. DeBeer, *J. Biol. Inorg. Chem.* **2016**, *21*, 793–805.
- [33] M. A. Beckwith, M. Roemelt, M.-N. Collomb, C. DuBoc, T.-C. Weng, U. Bergmann, P. Glatzel, F. Neese, S. DeBeer, *Inorg. Chem.* **2011**, *50*, 8397–8409.
- [34] N. Lee, T. Petrenko, U. Bergmann, F. Neese, S. DeBeer, *J. Am. Chem. Soc.* **2010**, *132*, 9715–9727.
- [35] S. Hugenbruch, H. S. Shafaat, T. Krämer, M. U. Delgado-Jaime, K. Weber, F. Neese, W. Lubitz, S. DeBeer, *Phys. Chem. Chem. Phys.* **2016**, *18*, 10688–10699.
- [36] V. Martin-Diaconescu, K. N. Chacón, M. U. Delgado-Jaime, D. Sokaras, T.-C. Weng, S. DeBeer, N. J. Blackburn, *Inorg. Chem.* **2016**, *55*, 3431–3439.
- [37] C. J. Pollock, S. DeBeer, *Acc. Chem. Res.* **2015**, *48*, 2967–2975.
- [38] C. J. Pollock, S. DeBeer, *J. Am. Chem. Soc.* **2011**, *133*, 5594–5601.
- [39] U. Bergmann, P. Glatzel, *Photosynth. Res.* **2009**, *102*, 255.
- [40] S. Lafuerza, J. García, G. Subías, J. Blasco, P. Glatzel, *Phys. Rev. B* **2016**, *93*, 205108.
- [41] G. E. Cutsail III, N. L. Gagnon, A. D. Spaeth, W. B. Tolman, S. DeBeer, *Angew. Chem. Int. Ed.* **2019**, *58*, 9114–9119; *Angew. Chem.* **2019**, *131*, 9212–9217.
- [42] G. Vankó, T. Neisius, G. Molnár, F. Renz, S. Kárpáti, A. Shukla, F. M. F. de Groot, *J. Phys. Chem. B* **2006**, *110*, 11647–11653.
- [43] F. M. F. de Groot, A. Fontaine, C. C. Kao, M. Krisch, *J. Phys. Condens. Matter* **1994**, *6*, 6875–6884.
- [44] A. M. March, T. A. Assefa, C. Bressler, G. Doumy, A. Galler, W. Gawelda, E. P. Kanter, Z. Németh, M. Pápai, S. H. Southworth, L. Young, G. Vankó, *J. Phys. Chem. C* **2015**, *119*, 14571–14578.
- [45] V. A. Safonov, L. N. Vykhodtseva, Y. M. Polukarov, O. V. Safonova, G. Smolentsev, M. Sikora, S. G. Eeckhout, P. Glatzel, *J. Phys. Chem. B* **2006**, *110*, 23192–23196.
- [46] H. Visser, E. Anxolabéhère-Mallart, U. Bergmann, P. Glatzel, J. H. Robblee, S. P. Cramer, J.-J. Girerd, K. Sauer, M. P. Klein, V. K. Yachandra, *J. Am. Chem. Soc.* **2001**, *123*, 7031–7039.
- [47] K. M. Lancaster, M. Roemelt, P. Ettenhuber, Y. Hu, M. W. Ribbe, F. Neese, U. Bergmann, S. DeBeer, *Science* **2011**, *334*, 974–977.
- [48] Y. Pushkar, X. Long, P. Glatzel, G. W. Brudvig, G. C. Dismukes, T. J. Collins, V. K. Yachandra, J. Yano, U. Bergmann, *Angew. Chem. Int. Ed.* **2010**, *49*, 800–803; *Angew. Chem.* **2010**, *122*, 812–815.
- [49] M. O. Krause, J. H. Oliver, *J. Phys. Chem. Ref. Data* **1979**, *8*, 329–338.
- [50] C. J. Pollock, M. U. Delgado-Jaime, M. Atanasov, F. Neese, S. DeBeer, *J. Am. Chem. Soc.* **2014**, *136*, 9453–9463.
- [51] S. Limandri, S. Ceppi, G. Tirao, G. Stutz, C. G. Sánchez, J. A. Riveros, *Chem. Phys.* **2010**, *367*, 93–98.
- [52] S. D. Gamblin, D. S. Urch, *J. Electron Spectrosc. Relat. Phenom.* **2001**, *113*, 179–192.
- [53] P. Glatzel, U. Bergmann, *Coord. Chem. Rev.* **2005**, *249*, 65–95.
- [54] F. de Groot, *Chem. Rev.* **2001**, *101*, 1779–1808.
- [55] M. U. Delgado-Jaime, S. DeBeer, M. Bauer, *Chem. Eur. J.* **2013**, *19*, 15888–15897.

- [56] T.-T. Lu, T.-C. Weng, W.-F. Liaw, *Angew. Chem. Int. Ed.* **2014**, *53*, 11562–11566; *Angew. Chem.* **2014**, *126*, 11746–11750.
- [57] P. V. Khadikar, N. F. Mangelson, S. P. Pandharkar, *Jpn. J. Appl. Phys.* **1989**, *28*, 709–712.
- [58] T. E. Westre, P. Kennepohl, J. G. DeWitt, B. Hedman, K. O. Hodgson, E. I. Solomon, *J. Am. Chem. Soc.* **1997**, *119*, 6297–6314.
- [59] D. V. Fomitchev, C. C. McLauchlan, R. H. Holm, *Inorg. Chem.* **2002**, *41*, 958–966.
- [60] R. Bjornsson, F. Neese, R. R. Schrock, O. Einsle, S. DeBeer, *J. Biol. Inorg. Chem.* **2015**, *20*, 447–460.
- [61] A. T. Thorhallsson, R. Bjornsson, *Inorg. Chem.* **2019**, *58*, 1886–1894.
- [62] R. Bjornsson, F. Neese, S. DeBeer, *Inorg. Chem.* **2017**, *56*, 1470–1477.
- [63] R. Bjornsson, M. U. Delgado-Jaime, F. A. Lima, D. Sippel, J. Schlesier, T. Weyhermüller, O. Einsle, F. Neese, S. DeBeer, *Z. Anorg. Allg. Chem.* **2015**, *641*, 65–71.
- [64] T. S. Hollingsworth, R. L. Hollingsworth, R. L. Lord, S. Groysman, *Dalton Trans.* **2018**, *47*, 10017–10024.

Manuscript received: March 10, 2020
Version of record online: May 29, 2020